

## Odd Nonlinear Conductivity under Spatial Inversion in Chiral Tellurium

Manuel Suárez-Rodríguez<sup>1</sup>, Beatriz Martín-García<sup>1,2</sup>, Witold Skowroński<sup>1,3</sup>, F. Calavalle<sup>1</sup>,  
Stepan S. Tsirkin<sup>2,4</sup>, Ivo Souza<sup>2,4</sup>, Fernando De Juan<sup>2,5</sup>, Andrey Chuvilin<sup>1,2</sup>, Albert Fert,<sup>5,6,7</sup>  
Marco Gobbi<sup>2,4,\*</sup>, Fèlix Casanova<sup>1,2,†</sup> and Luis E. Hueso<sup>1,2,‡</sup>

<sup>1</sup>CIC nanoGUNE BRTA, 20018 Donostia-San Sebastián, Basque Country, Spain

<sup>2</sup>IKERBASQUE, Basque Foundation for Science, 48009 Bilbao, Basque Country, Spain

<sup>3</sup>AGH University of Krakow, Institute of Electronics, 30-059 Kraków, Poland

<sup>4</sup>Centro de Física de Materiales CSIC-UPV/EHU, 20018 Donostia-San Sebastián, Basque Country, Spain

<sup>5</sup>Donostia International Physics Center, 20018 Donostia-San Sebastián, Basque Country, Spain

<sup>6</sup>Unité Mixte de Physique, CNRS, Thales, Université Paris-Saclay, 91767 Palaiseau, France

<sup>7</sup>Department of Materials Physics UPV/EHU, 20018 Donostia-San Sebastián, Basque Country, Spain



(Received 18 August 2023; accepted 13 December 2023; published 24 January 2024)

Electrical transport in noncentrosymmetric materials departs from the well-established phenomenological Ohm's law. Instead of a linear relation between current and electric field, a nonlinear conductivity emerges along specific crystallographic directions. This nonlinear transport is fundamentally related to the lack of spatial inversion symmetry. However, the experimental implications of an inversion symmetry operation on the nonlinear conductivity remain to be explored. Here, we report on a large, nonlinear conductivity in chiral tellurium. By measuring samples with opposite handedness, we demonstrate that the nonlinear transport is odd under spatial inversion. Furthermore, by applying an electrostatic gate, we modulate the nonlinear output by a factor of 300, reaching the highest reported value excluding engineered heterostructures. Our results establish chiral tellurium as an ideal compound not just to study the fundamental interplay between crystal structure, symmetry operations and nonlinear transport; but also to develop wireless rectifiers and energy-harvesting chiral devices.

DOI: [10.1103/PhysRevLett.132.046303](https://doi.org/10.1103/PhysRevLett.132.046303)

**Introduction.**—Ohm's law is one of the most established relations in physics and forms the basis of today's electronics. This phenomenological relation states that the charge current density ( $j$ ) in a material is linearly proportional to the applied electric field ( $E$ ) [1]. Under time-reversal symmetry conditions, most conducting materials follow this correlation down to the nanoscale [2], with a constant of proportionality which is the electrical conductivity of the system ( $\sigma$ ). However, and starting from recent seminal studies in WTe<sub>2</sub> [3–6], different experimental [7–15] and theoretical [16–22] reports showed that, in systems with broken inversion symmetry, a nonlinear charge current quadratically proportional to the applied electric field is allowed,  $\mathbf{j} = \sigma\mathbf{E} + \chi\mathbf{E}\mathbf{E}$  [23]. In this case, the proportionality is captured by the nonlinear susceptibility tensor of the system ( $\chi$ ), which depends on the symmetry of the material and may present both diagonal and off-diagonal components. On the one hand, off-diagonal components, which result on transverse responses leading to the nonlinear Hall effect, have attracted much attention as they are connected to the Berry curvature dipole [18]. On the other hand, fewer studies have been devoted to diagonal components, which are associated with the nonlinear longitudinal conductivity [24] and are purely connected to extrinsic mechanisms [18,25]. These components could lead to strong

nonlinear output signals promising for applications in frequency doubling [26,27], energy harvesting, and wireless detection via rectification [28–30].

Since breaking inversion symmetry is the fundamental requirement for the emergence of nonlinear transport, an inversion symmetry operation ( $i$ ) is expected to profoundly affect the nonlinear conductivity. However, the implications of such operation have not been experimentally explored so far. Indeed, the symmetry of the studied systems, mainly restricted to few-layer polar transition-metal dichalcogenides [31–33] and engineered noncentrosymmetric structures [34–40], does not permit us to distinguish the effect of  $i$  from that of a simple rotation.

Chiral materials have neither mirror planes nor inversion centers, and are, therefore, noncentrosymmetric. Unlike trivial rotations,  $i$  results in a change of handedness. In spite of their importance to test the effect of  $i$ , nonlinear conductivity has not been explored in any chiral material. In this regard, chiral elemental tellurium (Te), which can be synthesized on single-crystalline flakes with both handedness [41–44] and excellent electronic properties [45], represent an ideal platform to disentangle the effect of  $i$  and rotation on the nonlinear transport.

Here, we report the observation of a large nonlinear conductivity in chiral single-crystalline Te flakes. The

dependence of this nonlinear effect on the relative orientation between the crystallographic axes of Te and the current direction is fully explained by symmetry considerations, as it arises from the nonlinear susceptibility tensor of the space group of Te. By performing measurements on Te flakes with opposite handedness, we experimentally demonstrate that  $i$  changes the sign of the nonlinear tensor, in agreement with its spatial-inversion-odd nature. Moreover, the resistivity dependence of the nonlinear conductivity shows that side-jump scattering is its dominant microscopic mechanism. Finally, the electrostatic gating of the Te flakes allows us to tune its nonlinear response by a factor of 300, reaching a nonlinear voltage of up to 1.2 mV. This strong output signal, the highest reported excluding engineered heterostructures, opens the path to exploit chiral materials for wireless rectification and energy harvesting applications.

**Anisotropic transport.**—Elemental Te is the simplest material with a chiral structure. It is constituted by covalently bonded Te helices along the  $z$  axis, stacked together by van der Waals interactions. Single-crystalline Te flakes were grown by a hydrothermal process in the presence of a reducing agent. Tens-of-micrometers-long, few-micrometers-wide, and a hundred-nanometer-thick flakes were transferred onto Si/SiO<sub>2</sub> substrates using a Langmuir-Schaefer approach. We note that the flakes lie on the substrate with their  $x$  and chiral  $z$  axis in plane. In order to control the current direction and enable precise electrical measurements along the different crystal axes, the flakes were patterned in a starlike shape by reactive-ion etching, and contacted by sputtered Pt (see Supplemental Material, Sec. 1 [46]). Figure 1(a) shows the scanning electron microscopy (SEM) image of a typical device used in this study, with a sketch of the measurement configuration. A harmonic current,  $I^\omega$  (31 Hz) is injected between two electrodes which are along the same direction at an angle  $\theta$  from the chiral  $z$  axis, while both the longitudinal ( $V_{\parallel}$ ) and transverse ( $V_{\perp}$ ) voltages are measured in a rotating reference frame, meaning that all probes rotate simultaneously.

The temperature dependence of the first-harmonic longitudinal resistance along the crystal  $x$  axis ( $R_{xx}^\omega$ ) and  $z$  axis ( $R_{zz}^\omega$ ) is plotted in Fig. 1(b). The resistivity along the  $x$  axis is  $\sim 10$  times higher than along the  $z$  axis at room temperature, and it increases much more rapidly with decreasing temperature. This is a consequence of the anisotropic crystal structure of Te, with more favorable electronic transport along the covalently bonded Te helices, which are aligned along the chiral  $z$  axis. The first-harmonic voltage scales linearly with the current (Supplemental Material, Sec. 2 [46]). The slopes corresponding to the first-harmonic longitudinal [ $R_{\parallel}^\omega \equiv (V_{\parallel}^\omega/I^\omega)$ ] and transverse [ $R_{\perp}^\omega \equiv (V_{\perp}^\omega/I^\omega)$ ] resistances as a function of  $\theta$  at 10 K are presented in Fig. 1(c). Both show a twofold angular dependence, which is consistent with the crystal symmetry of Te and can be expressed as  $R_{\parallel}^\omega(\theta) = R_{zz}^\omega \cos^2\theta + R_{xx}^\omega \sin^2\theta$  and  $R_{\perp}^\omega(\theta) = (R_{xx}^\omega - R_{zz}^\omega) \cos\theta \sin\theta$ . The fit [dashed lines, Fig. 1(c)] yields a resistance anisotropy

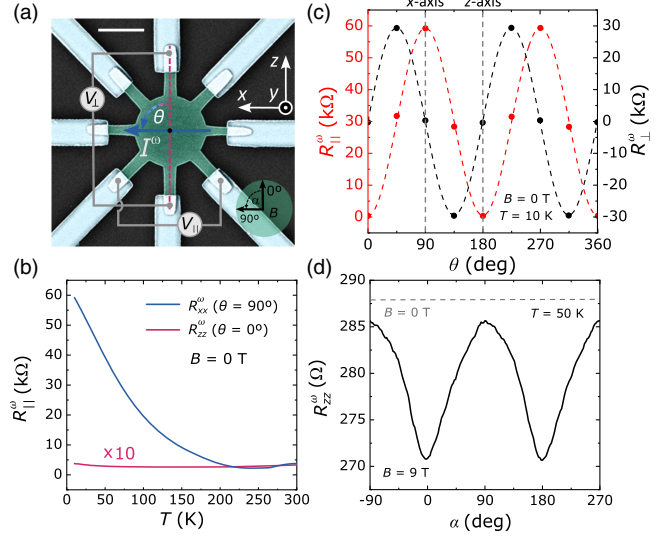


FIG. 1. Basic characterization of Te. (a) False-color SEM image of a typical starlike device used in this study. The etched Te flake (green) is contacted by Pt contacts (blue). The scale bar corresponds to 2  $\mu\text{m}$ . (b) Temperature dependence of the parallel first-harmonic resistance ( $R_{\parallel}^\omega$ ) when  $I^\omega$  is injected along the  $x$  and  $z$  axis. The data points for the latter are multiplied by 10 for clarity. (c) Parallel ( $R_{\parallel}^\omega$ ) and transverse ( $R_{\perp}^\omega$ ) first-harmonic resistance as a function of  $\theta$  at 10 K. The dashed lines are fits to the equations introduced in the main text. (d)  $\alpha$ -angle-dependent magnetoresistance of  $R_{zz}^\omega$  at 9 T and 50 K. The gray dashed line indicates the  $R_{zz}^\omega$  value at zero field. All data were measured in device S1.

$r[\equiv (R_{xx}/R_{zz})]$  of about 140. All measured devices display similar behavior (Supplemental Material, Sec. 3 [46]).

Figure 1(d) shows the angular-dependent magnetoresistance of  $R_{zz}^\omega$  obtained at 50 K by rotating an external magnetic field ( $B = 9$  T) an in-plane angle  $\alpha$ . The curves are characterized by minima at around  $\alpha = 0^\circ$  and  $\alpha = 180^\circ$ , that is, for  $B \parallel I_z$ , and maxima at around  $\alpha = \pm 90^\circ$ , for  $B \perp I_z$ . We note that the resistance measured at  $B = 0$  T, which is shown as a dashed line, is higher for all  $\alpha$  angles, indicating that the studied Te flakes present negative magnetoresistance for any in-plane direction of  $B$ , but stronger when it is aligned along the  $z$  axis.

**Nonlinear conductivity.**—The chiral structure of Te allows the generation of a second-order current density when an electric field is applied,  $\mathbf{j} = \sigma\mathbf{E} + \chi\mathbf{E}\mathbf{E}$ . That is, the nonlinear susceptibility tensor for the space groups of Te,  $P3_221$  (left-handed) or  $P3_121$  (right-handed) present nonvanishing elements [48]:

$$\chi = \begin{pmatrix} \chi_{xxx} & \chi_{xyy} & 0 & \chi_{xyz} & 0 & 0 \\ 0 & 0 & 0 & 0 & \chi_{yxz} & \chi_{yxy} \\ 0 & 0 & 0 & 0 & 0 & 0 \end{pmatrix}, \quad (1)$$

where  $\chi_{xxx} = -\chi_{xyy} = -\chi_{yxy}$  and  $\chi_{xyz} = -\chi_{yxz}$ . In our experimental setup, we measure the components in the

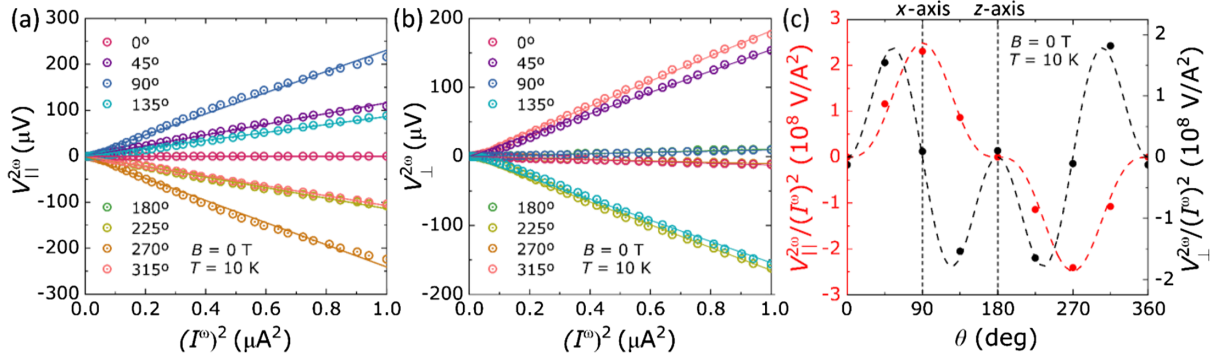


FIG. 2. Nonlinear conductivity. (a),(b) Second-order parallel  $V_{||}^{2\omega}$  (a) and transverse  $V_{\perp}^{2\omega}$  (b) voltage as a function of  $(I^\omega)^2$  at different  $\theta$  angles. The second-order voltage depends linearly on the square of  $I^\omega$ . (c) The nonlinear conductivity [slopes of the dependences in (a) and (b)] as a function of  $\theta$ . The dashed lines are fits to the experimental data with Eqs. (2) and (3). All measurements were performed in device S1 at 10 K.

$x-z$  plane [Fig. 1(a)]. Hence, we are sensitive to the diagonal component  $\chi_{xxx}$ , which acts as a correction to the Ohm's law along the  $x$  axis,  $j_x = \sigma_{xx}E_x^\omega + \chi_{xxx}E_x^\omega E_x^\omega$ . Therefore, when an electric field ( $E^\omega$ ) is applied along the  $x$  axis, a nonlinear current density is generated in the same direction [Fig. S3(a) [46]]. Conversely, when an electric field is applied along the  $z$  axis, the generation of a nonlinear charge current is forbidden by symmetry constraints, and therefore, Ohm's law holds,  $j_z = \sigma_{zz}E_z^\omega$  [Fig. S3(b) [46]].

For an in-plane ac current at an angle  $\theta$  from the chiral  $z$  axis, the nonlinear response through the second-order nonlinear susceptibilities can be expressed as follows (see Supplemental Material, Sec. 4 [46]):

$$\frac{V_{||}^{2\omega}}{(I^\omega)^2} = \frac{L_{||}}{L_x^3} A (R_{xx}^\omega)^3 \chi_{xxx} \sin^3(\theta), \quad (2)$$

$$\frac{V_{\perp}^{2\omega}}{(I^\omega)^2} = \frac{L_{\perp}}{L_x^3} A (R_{xx}^\omega)^3 \chi_{xxx} \sin^2(\theta) \cos(\theta), \quad (3)$$

where  $V_{||}^{2\omega}$  and  $V_{\perp}^{2\omega}$  are the second-harmonic voltages generated in a direction longitudinal and transverse to the current direction;  $L_{||}$ ,  $L_{\perp}$ , and  $L_x$  are the distances between contacts along the parallel direction, perpendicular direction, and  $x$  axis, respectively;  $A$  is the cross section. The equations take into account that, experimentally, we apply currents and measure voltages.

We highlight that we employ both a longitudinal and a transverse configuration to probe the diagonal component  $\chi_{xxx}$ , which describes the longitudinal nonreciprocal transport along the  $x$  axis. This is a unique feature that is fundamentally related to Te symmetry and proves the breakdown of Ohm's law. Moreover, the presence of just one component in Eqs. (2) and (3) allows us to fully determine its value. Previous studies employed the transverse (Hall) configuration to probe off-diagonal [4,8,9], but

also a combination of diagonal and off-diagonal components [5] of the nonlinear tensor. For this reason, the nonlinear transport is often referred to as nonlinear Hall effect.

We biased the disc device S1 with a harmonic current in a sequence along the 8 contacts rotated by  $45^\circ$ . The longitudinal,  $V_{||}^{2\omega}$  [Fig. 2(a)] and transverse,  $V_{\perp}^{2\omega}$  [Fig. 2(b)] second-harmonic voltages were recorded in a rotating reference frame. Both scale linearly with the square of the current, and switch sign when the current direction and the voltage probe connections are reversed simultaneously. The slopes of  $V_{||}^{2\omega}$  and  $V_{\perp}^{2\omega}$  normalized to  $(I^\omega)^2$  as a function of  $\theta$  are summarized in Fig. 2(c). Equations (2) and (3) perfectly capture the experimental angular dependence (dashed lines). From the two fittings, we obtain similar values of the nonlinear susceptibility component:  $\chi_{xxx} = (2.13 \pm 0.18) \times 10^{-3}$  and  $(2.49 \pm 0.18) \times 10^{-3} \Omega^{-1} \cdot \text{V}^{-1}$  from the longitudinal and transverse signals, respectively. Therefore, the experimental response is consistent with a nonlinear effect based on the symmetry of chiral Te.

*Spatial inversion operation.*—The operation of spatial inversion ( $i$ ), which is the combination of a twofold rotation with a perpendicular reflection, is fundamentally different from just a trivial rotation when applied to a chiral structure, as it introduces a change of handedness. Therefore, the Te flakes, which are synthesized as single crystals with both left and right handedness, allow us to directly explore the effect of  $i$  on the nonlinear conductivity [Fig. 3(a)]. We must point out that  $i$  in Te does not only change its handedness, but it also changes the orientation of the atomic triangles pattern that Te displays in the  $x-y$  plane. These triangular units can be imaged by scanning transmission electron microscopy (STEM), as shown in Fig. 3(a). Therefore, for comparing samples with different handedness and test the effect of  $i$ , we must align them with their atomic triangular pattern pointing to  $+x$  and  $-x$ , respectively.

We present the nonlinear conductivity in two Te devices with opposite handedness (device S1 and S2). Their

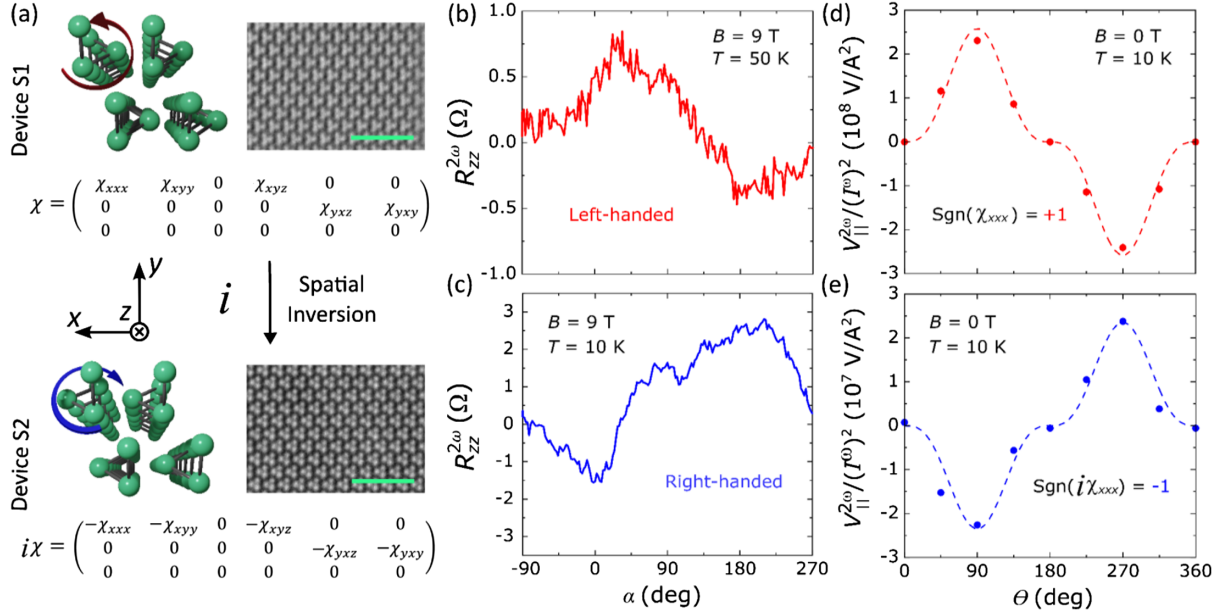


FIG. 3. Spatial inversion operation. (a) Spatial inversion operation over trigonal Te results on a change of handedness,  $180^\circ$  rotation of the  $x - y$  plane triangles pattern, and sign change of the nonlinear susceptibility tensor. STEM images of Te lamellas obtained by cutting perpendicular to the  $z$  axis devices S1 and S2 (scale bars correspond to 2 nm). (b),(c)  $\alpha$ -angle-dependent magnetoresistance of  $R_{zz}^{2\omega}$  at 9 T measured at 50 K in device S1 (b) and at 10 K in device S2 (c). The  $R_{zz}^{2\omega}$  signal determines that devices S1 and S2 are left- and right-handed, respectively. (d),(e) Nonlinear conductivity as a function of  $\theta$  at 10 K for device S1 (d) and S2 (e). The dashed lines are fits to the experimental data with Eq. (2). Data and fit in (d) are the same as in Fig. 2(c).

handedness was determined by measuring the unidirectional magnetoresistance (UMR), also known as electrical magnetochiral anisotropy [43]. The second-harmonic resistance along the  $z$  axis,  $R_{zz}^{2\omega}$ , as a function of the  $\alpha$  angle at 9 T gives us the UMR, showing a peak (valley) at  $\alpha = 0^\circ$  ( $\alpha = 180^\circ$ ) for device S1 [Fig. 3(b)] and a valley (peak) at  $\alpha = 0^\circ$  ( $\alpha = 180^\circ$ ) for device S2 [Fig. 3(c)]. The UMR in Te is a consequence of a chirality dependent Edelstein effect and confirms that devices S1 and S2 are left- and right-handed, respectively (see Supplemental Material, Sec. 5 [46]).

By imaging the Te  $x - y$  plane through STEM, we can orient the device S1 (left-handed) and S2 (right-handed) with their atomic triangular pattern pointing to  $+x$  and  $-x$ , respectively [STEM images in Fig. 3(a)]. We should highlight that the UMR measurement is independent on the orientation of the  $x$  axis, so that the handedness of Te flakes is determined unambiguously [49].

The nonlinear conductivity on devices S1 [Fig. 3(d)] and S2 [Fig. 3(e)] as a function of  $\theta$  [slopes of the dependences in Figs. 2(a) and S6(a) [46]] show for both the symmetry expected for Te [Eq. (2)], but opposite sign. Consequently, by measuring flakes with opposite handedness, we were able to demonstrate that the nonlinear susceptibility ( $\chi_{xxx}$ ) changes sign under spatial inversion, in agreement with its inversion-symmetry-odd nature. Therefore, the symmetry of chiral Te allowed us to directly probe the fundamental connection between nonlinear conductivity and broken inversion symmetry.

*Temperature and electrostatic gate dependences.*— Finally, we studied the microscopic mechanism of the nonlinear conductivity by observing its dependence on the resistivity of the material. The resistivity was modulated both by varying the sample temperature [Fig. 4(a)] and by applying an electrostatic gate voltage [Fig. 4(b)]. On the one hand, the resistivity increases while decreasing temperature, as also observed in Fig. 1(b). On the other hand, Te is a hole-doped semiconductor [45], therefore, its resistivity increases for positive gate voltages. For the same temperatures and gate voltages, we studied the nonlinear transverse voltage at  $\theta = 45^\circ$  and  $\theta = 135^\circ$ . As also observed in Fig. 3(b), it depends linearly on  $(I^\omega)^2$ . Its slope decreases while increasing temperature [Fig. S7(a) [46]], and it increases by applying positive gate voltages [Fig. S7(b) [46]]. The nonlinear conductivity as a function of the resistivity is plotted in Figs. 4(c) and 4(d). The scaling law between these two magnitudes can be formulated as [16,50]

$$\frac{V_{\perp}^{2\omega}}{(I^\omega)^2} = \beta + \gamma\rho_{xx} + \delta\rho_{xx}^2, \quad (4)$$

where  $\delta$  is an independent parameter, and  $\beta$  and  $\gamma$  only depend on the residual resistivity of the material. In time-reversal invariant systems, the only intrinsic contribution to the nonlinear susceptibility tensor is the Berry curvature dipole, which is captured by off-diagonal components [18,25]. Since we are probing  $\chi_{xxx}$  (diagonal component),

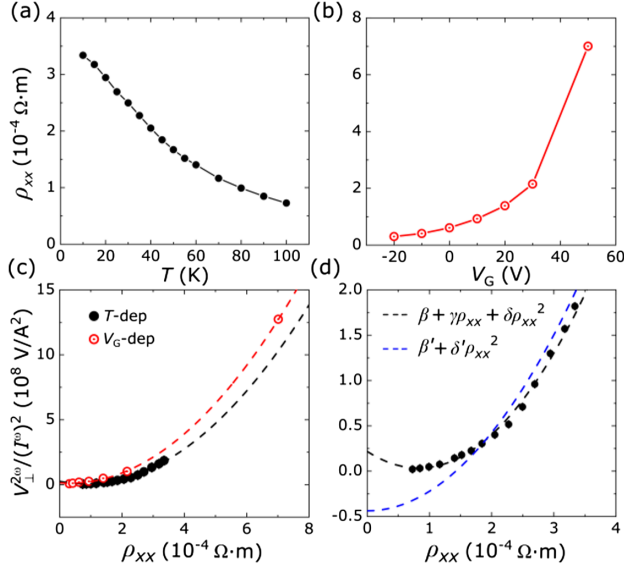


FIG. 4. (a) Temperature and (b) gate dependence of the resistivity along the  $x$  axis ( $\rho_{xx}$ ). (c) The nonlinear conductivity [taken from the slopes of  $V_{\perp}^{2\omega}$  as a function of  $(I^{\omega})^2$  at  $\theta = 45^\circ$  in Figs. S7(a) and S7(b) [46]] as a function of  $\rho_{xx}$ , tuned by either temperature (solid black circles) or gate (open red circles). The dashed lines are fits to experimental data with Eq. (4). (d) Comparison between fits to Eq. (4) with (black dashed line) and without (blue dashed line) the linear term ( $\gamma$ ) for the temperature-tuned dataset.

the measured effect cannot have an intrinsic origin. The fit to Eq. (4) [dashed lines in Figs. 4(c) and 4(d)] reveals a nonmonotonic behavior of  $V_{\perp}^{2\omega}/(I^{\omega})^2$  versus  $\rho_{xx}$ , where  $V_{\perp}^{2\omega}/(I^{\omega})^2$  first decreases and then increases. This requires the linear and quadratic coefficients to have different signs [Fig. 4(d)]. The existence of a linear term in  $\rho_{xx}$  with opposite sign can only be consistent with a mechanism involving side-jump scattering from dynamic sources (see detailed analysis in Supplemental Material, Sec. 7 [46]). Moreover, the similar temperature and gate dependence of the observed nonlinear conductivity evidences a negligible contribution from a displacement field when applying an electrostatic gate voltage. Therefore, the strong intrinsic low symmetry of chiral Te is not substantially affected by the presence of an out-of-plane electric field.

Besides the fundamental connection between the nonlinear conductivity in chiral Te and the side-jump microscopic mechanism, the electrostatic gate allows us to modulate the second-harmonic voltage output by a factor of 300, reaching a value of 1.2 mV for 1  $\mu$ A input current [Fig. 4(c)]. Although the nonlinear susceptibility components would be the most appropriate quantities to compare between different systems, they are not reported in previous literature. Therefore, and because of its potential importance in energy harvesting applications, we highlight that our voltage output is the highest reported excluding engineered heterostructures [Fig. S9 [46]].

To conclude, we directly observed nonlinear conductivity along the  $x$  axis of chiral Te, which is odd under spatial inversion and the largest reported in a single material. Its resistivity dependence unveils side-jump scattering as the dominant microscopic mechanism.

We thank Talieh S. Ghiasi for valuable insights regarding the device fabrication process. This work is supported by the Spanish MCIU/AEI/10.13039/501100011033 and by ERDF A way of making Europe (Projects No. PID2021-122511OB-I00, No. PID2021-128760NB-I00, No. PID2021-129035NB-I00, and “Maria de Maeztu” Units of Excellent Programme No. CEX2020-001038-M). M. S.-R. acknowledges support from La Caixa Foundation (No. 100010434) with code LCF/BQ/DR21/11880030. B.M.-G. and M.G. thank support from the “Ramón y Cajal” Programme by the Spanish MCIU/AEI (Grants No. RYC2021-034836-I and No. RYC2021-031705-I). W.S. thanks Grant No. PPN/BEK/2020/1/00118/DEC/1 from the Polish National Agency for Academic Exchange. A.F. acknowledges the support of the UNIVERSIDAD DEL PAIS VASCO as distinguished researcher.

\*Corresponding author: marco.gobbi@ehu.eus

†Corresponding author: f.casanova@nanogune.eu

‡Corresponding author: lhueso@nanogune.eu

- [1] D. J. Griffiths, *Introduction to Electrodynamics* (Pearson, Boston, 1942).
- [2] B. Weber *et al.*, Ohm’s law survives to the atomic scale, *Science* **335**, 64 (2012).
- [3] Y. Zhang, J. van den Brink, C. Felser, and B. Yan, Electrically tuneable nonlinear anomalous Hall effect in two-dimensional transition-metal dichalcogenides  $\text{WTe}_2$  and  $\text{MoTe}_2$ , *2D Mater.* **5**, 044001 (2018).
- [4] Q. Ma *et al.*, Observation of the nonlinear Hall effect under time-reversal-symmetric conditions, *Nature (London)* **565**, 337 (2019).
- [5] K. Kang, T. Li, E. Sohn, J. Shan, and K. F. Mak, Nonlinear anomalous Hall effect in few-layer  $\text{WTe}_2$ , *Nat. Mater.* **18**, 324 (2019).
- [6] J. Xiao *et al.*, Berry curvature memory through electrically driven stacking transitions, *Nat. Phys.* **16**, 1028 (2020).
- [7] S.-C. Ho, C.-H. Chang, Y.-C. Hsieh, S.-T. Lo, B. Huang, T.-H.-Y. Vu, C. Ortix, and T.-M. Chen, Hall effects in artificially corrugated bilayer graphene without breaking time-reversal symmetry, *Nat. Electron.* **4**, 116 (2021).
- [8] A. Tiwari *et al.*, Giant  $c$ -axis nonlinear anomalous Hall effect in  $\text{T}_d$  –  $\text{MoTe}_2$  and  $\text{WTe}_2$ , *Nat. Commun.* **12**, 2049 (2021).
- [9] T. Ma *et al.*, Growth of bilayer  $\text{MoTe}_2$  single crystals with strong nonlinear Hall effect, *Nat. Commun.* **13**, 5465 (2022).
- [10] Y. M. Itahashi, T. Ideue, S. Hoshino, C. Goto, H. Namiki, T. Sasagawa, and Y. Iwasa, Giant second harmonic transport under time-reversal symmetry in a trigonal superconductor, *Nat. Commun.* **13**, 1659 (2022).

- [11] O. O. Shvetsov, V. D. Esin, A. V. Timonina, N. N. Kolesnikov, and E. V. Deviatov, Nonlinear Hall effect in three-dimensional Weyl and Dirac semimetals, *JETP Lett.* **109**, 715 (2019).
- [12] M.-S. Qin, P.-F. Zhu, X.-G. Ye, W.-Z. Xu, Z.-H. Song, J. Liang, K. Liu, and Z.-M. Liao, Strain tunable Berry curvature dipole, orbital magnetization and nonlinear Hall effect in WSe<sub>2</sub> monolayer, *Chin. Phys. Lett.* **38**, 017301 (2021).
- [13] S. Dzsaber *et al.*, Giant spontaneous Hall effect in a nonmagnetic Weyl-Kondo semimetal, *Proc. Natl. Acad. Sci. U.S.A.* **118**, e2013386118 (2021).
- [14] T. Nishijima, T. Watanabe, H. Sekiguchi, Y. Ando, E. Shigematsu, R. Ohshima, S. Kuroda, and M. Shiraishi, Ferroic Berry curvature dipole in a topological crystalline insulator at room temperature, *Nano Lett.* **23**, 2247 (2023).
- [15] L. Min *et al.*, Colossal nonreciprocal Hall effect and broadband frequency mixing due to a room temperature nonlinear Hall effect, [arXiv:2303.03738](https://arxiv.org/abs/2303.03738).
- [16] Z. Z. Du, C. M. Wang, S. Li, H.-Z. Lu, and X. C. Xie, Disorder-induced nonlinear Hall effect with time-reversal symmetry, *Nat. Commun.* **10**, 3047 (2019).
- [17] Z. Z. Du, C. M. Wang, H. P. Sun, H.-Z. Lu, and X. C. Xie, Quantum theory of the nonlinear Hall effect, *Nat. Commun.* **12**, 5038 (2021).
- [18] I. Sodemann and L. Fu, Quantum nonlinear Hall effect induced by Berry curvature dipole in time-reversal invariant materials, *Phys. Rev. Lett.* **115**, 216806 (2015).
- [19] S. Nandy and I. Sodemann, Symmetry and quantum kinetics of the nonlinear Hall effect, *Phys. Rev. B* **100**, 195117 (2019).
- [20] R. H. Li, O. G. Heinonen, A. A. Burkov, and S. S.-L. Zhang, Nonlinear Hall effect in Weyl semimetals induced by chiral anomaly, *Phys. Rev. B* **103**, 045105 (2021).
- [21] C. Wang, Y. Gao, and D. Xiao, Intrinsic nonlinear Hall effect in antiferromagnetic tetragonal CuMnAs, *Phys. Rev. Lett.* **127**, 277201 (2021).
- [22] H. Liu, J. Zhao, Y. X. Huang, W. Wu, X. L. Sheng, C. Xiao, and S. A. Yang, Intrinsic second-order anomalous Hall effect and its application in compensated antiferromagnets, *Phys. Rev. Lett.* **127**, 277202 (2021).
- [23] Z. Z. Du, H.-Z. Lu, and X. C. Xie, Nonlinear Hall effects, *Nat. Rev. Phys.* **3**, 744 (2021).
- [24] P. He, G. K. Wai Koon, H. Isobe, J. Y. Tan, J. Hu, A. H. Castro Neto, L. Fu, and H. Yang, Graphene moiré superlattices with giant quantum nonlinearity of chiral Bloch electrons, *Nat. Nanotechnol.* **17**, 378 (2022).
- [25] S. S. Tsirkin and I. Souza, On the separation of Hall and Ohmic nonlinear responses, *SciPost Phys. Core* **5**, 039 (2022).
- [26] P. He, H. Isobe, D. Zhu, C.-H. Hsu, L. Fu, and H. Yang, Quantum frequency doubling in the topological insulator Bi<sub>2</sub>Se<sub>3</sub>, *Nat. Commun.* **12**, 698 (2021).
- [27] L. Min *et al.*, Strong room-temperature bulk nonlinear Hall effect in a spin-valley locked Dirac material. *Nat. Commun.* **14**, 364 (2023).
- [28] D. Kumar, C.-H. Hsu, R. Sharma, T.-R. Chang, P. Yu, J. Wang, G. Eda, G. Liang, and H. Yang, Room-temperature nonlinear Hall effect and wireless radiofrequency rectification in Weyl semimetal TaIrTe<sub>4</sub>, *Nat. Nanotechnol.* **16**, 421 (2021).
- [29] Y. Zhang and L. Fu, Terahertz detection based on nonlinear Hall effect without magnetic field, *Proc. Natl. Acad. Sci. U.S.A.* **118**, e2100736118 (2021).
- [30] C. Guo, Z. Chen, X. Yu, L. Zhang, X. Wang, X. Chen, and L. Wang, Ultrasensitive anisotropic room-temperature terahertz photodetector based on an intrinsic magnetic topological insulator MnBi<sub>2</sub>Te<sub>4</sub>, *Nano Lett.* **22**, 7492 (2022).
- [31] B. T. Zhou, C.-P. Zhang, and K. T. Law, Highly tunable nonlinear Hall effects induced by spin-orbit couplings in strained polar transition-metal dichalcogenides, *Phys. Rev. Appl.* **13**, 024053 (2020).
- [32] S. Lai *et al.*, Third-order nonlinear Hall effect induced by the Berry-connection polarizability tensor, *Nat. Nanotechnol.* **16**, 869 (2021).
- [33] X.-G. Ye, H. Liu, P. F. Zhu, W. Z. Xu, S. A. Yang, N. Shang, K. Liu, and Z. M. Liao, Control over Berry curvature dipole with electric field in WTe<sub>2</sub>, *Phys. Rev. Lett.* **130**, 016301 (2023).
- [34] L. Du, T. Hasan, A. Castellanos-Gomez, G.-B. Liu, Y. Yao, C. Ning Lau, and Z. Sun, Engineering symmetry breaking in 2D layered materials, *Nat. Rev. Phys.* **3**, 193 (2021).
- [35] M. Huang *et al.*, Giant nonlinear Hall effect in twisted bilayer WSe<sub>2</sub>, *Natl. Sci. Rev.* **10**, nwac232 (2023).
- [36] J. Duan, Y. Jian, Y. Gao, H. Peng, J. Zhong, Q. Feng, J. Mao, and Y. Yao, Giant second-order nonlinear Hall effect in twisted bilayer graphene, *Phys. Rev. Lett.* **129**, 186801 (2022).
- [37] S. Sinha *et al.*, Berry curvature dipole senses topological transition in a moiré superlattice, *Nat. Phys.* **18**, 765 (2022).
- [38] K. Kang, W. Zhao, Y. Zeng, K. Watanabe, T. Taniguchi, J. Shan, and K. F. Mak, Switchable moiré potentials in ferroelectric WTe<sub>2</sub>/WSe<sub>2</sub> superlattices, *Nat. Nanotechnol.* **18**, 861 (2023).
- [39] M. Huang *et al.*, Intrinsic nonlinear Hall effect and gate-switchable Berry curvature sliding in twisted bilayer graphene, *Phys. Rev. Lett.* **131**, 066301 (2023).
- [40] N. J. Zhang *et al.*, Angle-resolved transport nonreciprocity and spontaneous symmetry breaking in twisted trilayer graphene, [arXiv:2209.12964](https://arxiv.org/abs/2209.12964).
- [41] A. Ben-Moshe *et al.*, The chain of chirality transfer in tellurium nanocrystals, *Science* **372**, 729 (2021).
- [42] Z. Dong and Y. Ma, Atomic-level handedness determination of chiral crystals using aberration-corrected scanning transmission electron microscopy, *Nat. Commun.* **11**, 1588 (2020).
- [43] F. Calavalle *et al.*, Gate-tuneable and chirality-dependent charge-to-spin conversion in tellurium nanowires, *Nat. Mater.* **21**, 526 (2022).
- [44] A. Roy, F. T. Cerasoli, A. Jayaraj, K. Tenzin, M. B. Nardelli, and J. Sławińska, Long-range current-induced spin accumulation in chiral crystals, *npj Comput. Mater.* **8**, 243 (2022).
- [45] Y. Wang *et al.*, Field-effect transistors made from solution-grown two-dimensional tellurene, *Nat. Electron.* **1**, 228 (2018).
- [46] See Supplemental Material at <http://link.aps.org/supplemental/10.1103/PhysRevLett.132.046303> for methods details, further experimental data, and detailed theoretical analysis, which includes Ref. [47].

- [47] P. He, S. S.-L. Zhang, D. Zhu, Y. Liu, Y. Wang, J. Yu, G. Vignale, and H. Yang, Bilinear magnetoelectric resistance as a probe of three-dimensional spin texture in topological surface states, *Nat. Phys.* **14**, 495 (2018).
- [48] S. V. Gallego, J. Etxebarria, L. Elcoro, E. S. Tasci, and J. M. Perez-Mato, Automatic calculation of symmetry-adapted tensors in magnetic and non-magnetic materials: A new tool of the Bilbao Crystallographic Server, *Acta Crystallogr. Sect. B* **75**, 438 (2019).
- [49] X. Liu, I. Souza, and S. S. Tsirkin, Electrical magnetochiral anisotropy in trigonal tellurium from first principles, *arXiv: 2303.10164*.
- [50] D. Hou, G. Su, Y. Tian, X. Jin, S. A. Yang, and Q. Niu, Multivariable scaling for the anomalous Hall effect, *Phys. Rev. Lett.* **114**, 217203 (2015).